A novel computer-aided diagnosis system for the early detection of hypertension based on cerebrovascular alterations

Heba Kandil[a,b], Ahmed Soliman[a], Fatma Taher[c], Mohammed Ghazal[d], Ashraf Khalil[d], Guruprasad Giridharan[a], Robert Keynton[a], J. Richard Jennings[e], Ayman El-Baz[*,a]

[a] Bioimaging Laboratory, J.B Speed School of Engineering, University of Louisville, KY, USA
[b] Information Technology Department, Faculty of Computer Science and Information, Mansoura University, Egypt
[c] Zayed University, Dubai, UAE
[d] Electrical and Computer Engineering Department, Abu Dhabi University, UAE
[e] Department of Psychiatry and Psychology, University of Pittsburgh, PA, USA

ABSTRACT

Hypertension is a leading cause of mortality in the USA. While simple tools such as the sphygmomanometer are widely used to diagnose hypertension, they could not predict the disease before its onset. Clinical studies suggest that alterations in the structure of human brains' cerebrovasculature start to develop years before the onset of hypertension. In this research, we present a novel computer-aided diagnosis (CAD) system for the early detection of hypertension. The proposed CAD system analyzes magnetic resonance angiography (MRA) data of human brains to detect and track the cerebral vascular alterations and this is achieved using the following steps: i) MRA data are preprocessed to eliminate noise effects, correct the bias field effect, reduce the contrast inhomogeneity using the generalized Gauss-Markov random field (GGMRF) model, and normalize the MRA data, ii) the cerebral vascular tree of each MRA volume is segmented using a 3-D convolutional neural network (3D-CNN), iii) cerebral features in terms of diameters and tortuosity of blood vessels are estimated and used to construct feature vectors, iv) feature vectors are then used to train and test various artificial neural networks to classify data into two classes; normal and hypertensive. A balanced data set of 66 subjects were used to test the CAD system. Experimental results reported a classification accuracy of 90.9% which supports the efficacy of the CAD system components to accurately model and discriminate between normal and hypertensive subjects. Clinicians would benefit from the proposed CAD system to detect and track cerebral vascular alterations over time for people with high potential of developing hypertension and to prepare appropriate treatment plans to mitigate adverse events.

1. Introduction

One in every three adults in the USA are afflicted with hypertension. Clinical studies have suggested that hypertension damages and changes the structure of the human brain vasculature (Iadecola and Davisson, 2008; Soler et al., 1998). Change in cerebral structures contributes to the development of strokes, dementia, brain lesions, cognitive impairment, and ischemic cerebral injury (Iadecola and Davisson, 2008). Clinical hypotheses suggest that cerebral alterations start to develop before the symptomatic onset of hypertension. In particular, there are suggestions that there is a correlation between alterations in diameters and tortuosity of cerebral blood vessels and the development of hypertension. In 2016, Warnert et al., published a study that is considered the first confirmation for the hypothesis that cerebral vasculature and

cerebral perfusion pressure changes may be significant factors in the development of hypertension (Warnert et al., 2016). Their study supported the higher prevalence of congenital cerebrovascular changes in hypertensive subjects than normotensive subjects. These cerebral alterations result in an increase in the cerebrovascular resistance and the cerebral perfusion pressure. In their study, the authors discovered that cerebral remodeling was found in patients with high-normal- blood pressure (pre-hypertensive) who have a family history of developing hypertension. This would potentially mean that these alterations were not caused by hypertension but may be a cause for developing hypertension. The study indicates that hypertension might be developed to maintain balance in blood circulation of human brains to compensate the imbalance caused by the cerebral vascular alterations. In addition, other studies suggest that cerebral vascular remodeling and elevated

cerebral perfusion pressure precede the onset of hypertension in animals and humans (Barnes et al., 2017; Cates et al., 2012; Launer et al., 2015; Swales, 1991). Chronic elevation of blood pressure has been linked to carotid artery diameter change in rats (Hayashi et al., 2018). Pulmonary hypertension has been linked to pulmonary arterial diameters changes in humans. Clinical observations of excessive or abnormal tortuosity of blood vessels have been linked to several severe diseases including hypertension (Abdalla et al., 2015; Han, 2012; Hiroki et al., 2002; Jakob et al., 1996). The early detection of these vascular alterations would potentially help clinicians to prepare medical treatment plans and recommend healthier lifestyles that could prevent or limit the progression of the disease.

Time-of-flight magnetic resonance angiography (TOF-MRA) is currently used to best visualize human brains' cerebrovasculature. It is considered one of the most common imaging modalities used in non-invasive vascular research. However, developing an automatic segmentation algorithm to delineate cerebral vascular tree from MRA data accurately is still challenging. Specifically, cerebrovascular segmentation algorithms introduced in literature have limitations in segmenting vessels of small size. This is due to the complex geometry of human brains, scanning artifacts and limitations, wide range of intensities, density and diameters of small blood vessels ($\leq$ 1 mm), and the brain's fat tissues which have a similar visual appearance to that's of cerebral blood vessels. Additionally, manual segmentation or semi-automatic segmentation approaches which require human operator interactions are very time-consuming, error-prone, and subject to inter-observer variability. MRA-based computer-aided diagnosis (CAD) systems were introduced in literature to help radiologists in the clinical diagnoses of various diseases (Arimura et al., 2004; 2006; Doi, 2007; Fujita et al., 2008; Kobashi et al., 2006; Miki et al., 2016; Nakao et al., 2018). An MRA-based CAD system was presented in Fujita et al. (2008) to early detect lacunar infarcts, unruptured aneurysms, and arterial occlusions from MRA data. Another CAD system used unenhanced MRA images to detect cerebral aneurysms (Nakao et al., 2018). MRA data were analyzed using a CAD system in Miki et al. (2016) to detect small intracranial aneurysms. In this manuscript, we present an MRA-based CAD system for the early detection of hypertension. While simple tools such as the sphygmomanometer are widely used to diagnose hypertension, they could not predict the disease before its onset. The essential motivation behind this research was to help clinicians to predict pre-hypertension or hypertension before their onset to minimize or avoid any adverse events.

2. Methodology

The proposed CAD system, (Fig. 1), is composed of four main modules. The first module is responsible for data preprocessing to remove noise artifacts and enhance image homogeneity. The second module is responsible for delineating the cerebral vasculature using a 3-D convolutional neural network (3-D CNN). The third module extracts cerebral features from the segmented vasculature and builds a feature vector for each subject in the data set. The last module is responsible for the classification of input subjects into normal and hypertensive classes.

2.1. Materials and procedure

A balanced TOF-MRA dataset of 66 subjects, (33 subjects were normotensive, and 33 subjects were either pre-hypertensive or hypertensive), were used in the experimentation. According to the 2017 guideline, an update of the 2003 Seventh Report of the Joint National Committee on Prevention, Detection, Evaluation, and Treatment of High Blood Pressure (JNC7), the recommendations for hypertension categories based on the blood pressure measurements are as follow; normal ($<$ 120/ $<$ 80 mmHg), elevated or pre-hypertension (120 − 129/<80 mmHg), hypertension stage 1 (130 − 139 mmHg systolic or 80 − 89 mmHg diastolic), and hypertension stage 2

($\geq$ 140 mmHg systolic or $\geq$ 90 mmHg diastolic)(Chobanian et al., 2003; Whelton et al., 2018). So, in our experiment, a typical normotensive subject should have a systolic blood pressure of $<$ 120 mmHg and a diastolic blood pressure of $<$ 80 mmHg, while a hypertensive subject should have a systolic blood pressure of $>$ 130 mmHg or a diastolic blood pressure of $>$ 80 mmHg. In this study, a pre-hypertensive patient is defined to have elevated blood pressure measurements of (120 − 129) mmHg systolic and $<$ 80 mmHg diastolic. Patient recruitment and data collection were performed at University of Pittsburgh with local Institutional Review Board (IRB) approval and in accordance with relevant guidelines and regulations. Participants provided informed consent prior to any study data being collected. MRA scans were acquired using a 3T Trio TIM scanner using a 12-channel phased-array head coil. Each data volume consisted of 136 slices of thickness 0.5 mm and a matrix of 696 x 768 with in-plane spacing of 0.26 mm. Four readings of blood pressure were taken for each subject using a sphygmomanometer during two visits and were averaged. Further details on the study from which these participants were drawn is presented in Jennings et al. (2017). De-identified MRA data and associated blood pressure measurements were provided to the authors at University of Louisville for analysis. The image processing team had no contact with patients or access to protected health information.

2.2. Data preparation

MRA data were first preprocessed to enhance the segmentation accuracy. A non-parametric bias correction algorithm (Tustison et al., 2010) was applied on MRA data to remove any biasing effects and to correct any intensity non-uniformities. A 3-D generalized Gauss-Markov random field (GGMRF) (Bouman and Sauer, 1993) was then applied where the pairwise interactions between a voxel and its 26-neighborhood voxels were taken into consideration to enhance data homogeneity while preserving the 3-D edges between different cerebral structures (Fig. 2). At last, a normalization step was applied where the intensities of each MRA slice were manipulated to have a zero-mean and a unit-variance. Normalization was needed to facilitate a faster convergence of the CNN segmentation process.

2.3. Segmentation of brain vasculature using a 3-D CNN

The cerebral vasculature of each subject was segmented using a deep 3-D CNN. The architecture of the CNN consists of 11 layers to ensure a high degree of discrimination. The receptive field was of size 17^3. The task of feature extraction was performed using 3^3 kernels in each layer. The classification layer had 1^3 kernel. The segmentation task was performed in two steps. In the first step, adjacent image patches were densely trained into one pass of the network. Images were processed at multiple scales simultaneously to incorporate local and textual information to enhance the segmentation accuracy. The soft segmentation maps were generated as outputs for this step. In the second step, the soft segmentation maps were processed using a 3-D fully-connected conditional random field (CRF) to get rid of false positives.

As the spatial context for each voxel is taken into account, the final segmentation maps produced by the CNN are almost smooth. However, to overcome the local minima in the training and noise in the input images that may produce false positives or holes in the prediction, the fully connected CRF (Kamnitsas et al., 2017) was used as a post processing to achieve enhanced segmentation. Given an input image I, and the segmentation map, m, the Gibbs energy in a CRF model is given by:-

$$E(\mathbf{m}) = \sum_i \psi_u(m_i) + \sum_{ij,i \neq j} \psi_p(m_i, m_j)$$

(1)

The unary potential $\psi_i(m_i) = -logP(m_i|\mathbf{I})$ and $logP(m_i|\mathbf{I})$ is the CNN's output for voxel i. The pairwise potential in the fully connected CRF is of the form $\psi_p(m_i, m_j) = \mu(m_i, m_j)k(\mathbf{f}_i, \mathbf{f}_j)$ between any pair of voxels.
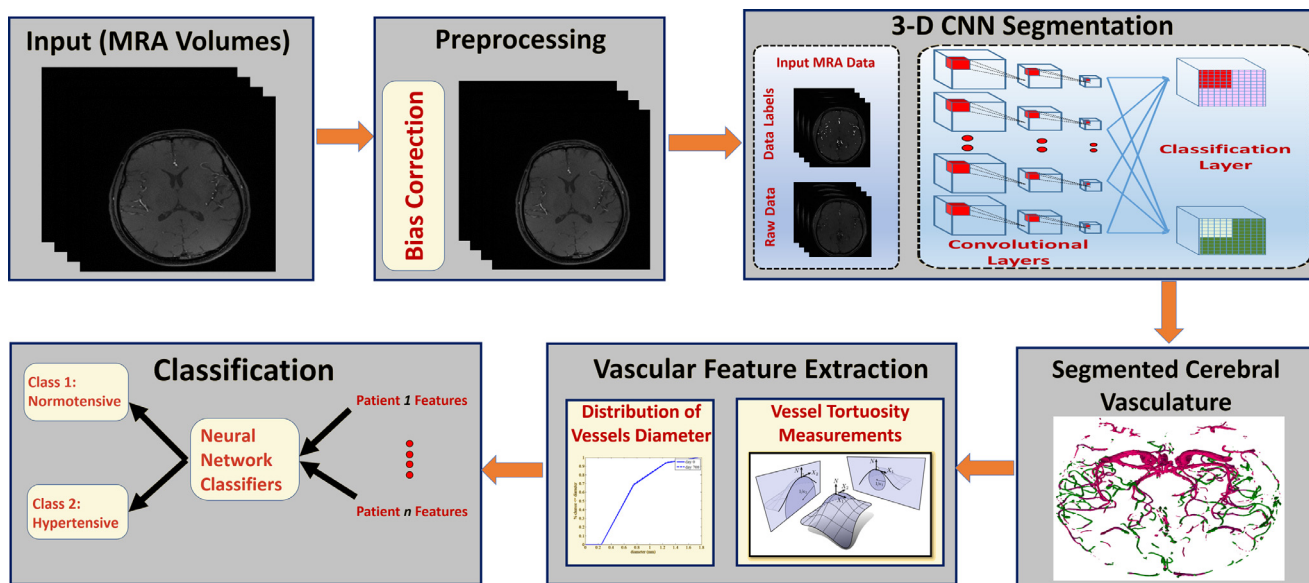
Fig. 1. A computer-aided-diagnosis system for the early detection of hypertension

The label compatibility, $\mu(m_i, m_j)$ is calculated using the Pott's model and the corresponding energy penalty is given by the function k, that is defined over arbitrary feature space with $\mathbf{f}_i$, $\mathbf{f}_j$ being the feature vector of the voxel pairs (Kamnitsas et al., 2017). For more details please see Kamnitsas et al. (2017); Krähenbühl and Koltun (2011).

The 3-D CNN architecture consists of eight layers, two fully connected layers, and one classification layer. The kernel size is 3^3 and the number of feature maps (FMs) at the eight layers are 30,30,40,40,40,40,50,50. The input to the network are image segments with size 25 x 25 x 25 and the batch size is 10 segments. The strides are unary and no pooling layers were used as it leads to loss of the voxel's exact position and therefore affects the accuracy negatively. The architecture uses the PReLu non-linearity and trained using the RMSProp optimizer and Nesterov momentum with values $L_1 = 10^{-6}$, $L_2 = 10^{-4}$, and $m = 0.6$. The learning rate is set to 10^{-3} and the dropout with 50% rate was employed on the last hidden layers. The batch normalization technique (Ioffe and Szegedy, 2015; Kamnitsas et al., 2017) for all hidden layers was used to allow the normalization of the FM activation at every optimization step.

The strength of the signals of blood flow at a specific time differs from one area to another inside the brain. To address this challenge, we had to partition each MRA volume into two compartments such that blood vessels inside each compartment are of similar appearance, shape, and approximate diameter size. This would potentially enhance the accuracy and efficiency of the segmentation process. We have selected a well-known cerebral bio-marker called circle of Willis (CoW) to

guide us during the partitioning process. Usually, most of the blood vessels existing at CoW and below it are of medium or large diameter size (1 mm: 25 mm), while blood vessels above CoW tend to have smaller diameter size (0.01 mm : 1 mm). Based on that, the first compartment included all MRA slices located above CoW, while the second compartment included all slices located at and below CoW. In each compartment, all the blood vessels tend to have similar appearance, shape, and diameters of approximate sizes which would increase the efficiency and accuracy of the segmentation process. During this process, the 3-D CNN manipulated each compartment and produced a subvascular tree. The two sub-vascular trees were combined later to obtain the final vascular tree.

2.4. Vascular features extraction

The delineated cerebral vasculature of each subject was used to extract a set of discriminative features, namely, the vascular diameter and tortuosity. These features were carefully selected to represent cerebral vasculature of each subject in the diagnosis phase based on clinical suggestions. Research studies have supported the correlation between the change in vascular diameter and hypertension (Lange et al., 2013; Ussavarungsi et al., 2014). Similarly, tortuosity of blood vessels, which measures how sharply a blood vessel twists or bends, has been linked to many diseases including hypertension (Han, 2012). To estimate the alterations in the diameters of blood vessels, the vascular radius was calculated for every cerebral vessel. The distance map was
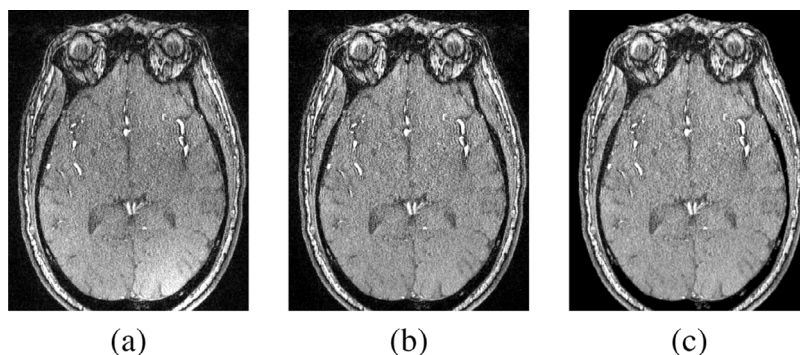

Fig. 2. A sample 2-D output of the preprocessing stage. (a) Original axial slice, (b) Output after bias correction, and (c) Output after GGMRF application on the bias-corrected slice.
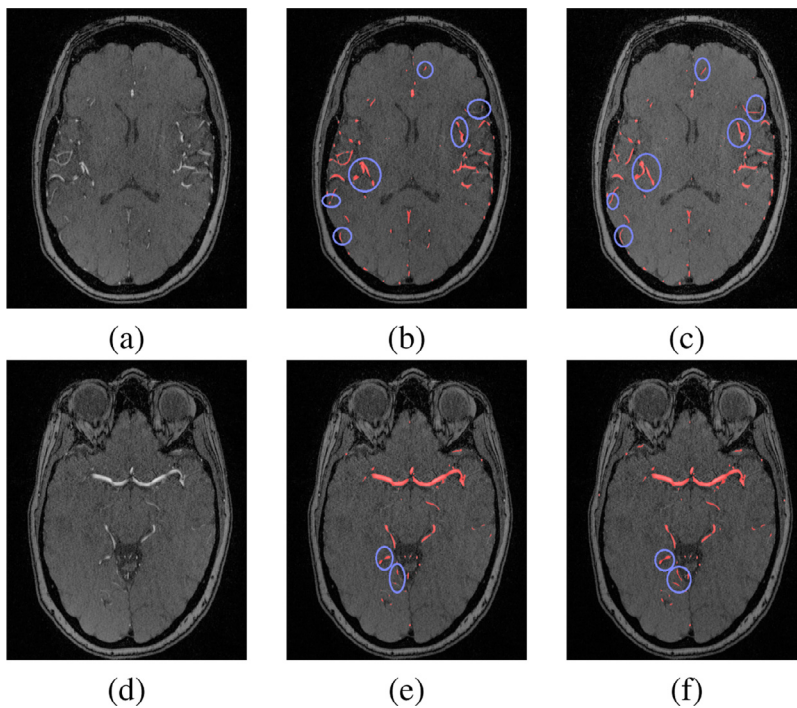
Fig. 3. A 2-D segmentation output of global and local experiments at two different cross sections above CoW (a,b,c) and below CoW (d,e,f). (a) and (d) Original slices, (b) and (e) Output of global segmentation, and (c) and (f) Output of local segmentation. Segmented vessels are colored in red and the enhanced segmentation results (of the local experiment) are contoured in blue. (For interpretation of the references to colour in this figure legend, the reader is referred to the web version of this article.)

generated for the segmented cerebral vasculature and was then used to estimate the probability distribution function (PDF) for each cerebral vascular tree of every subject. To estimate the change in cerebral vascular tortuosity, mean and Gaussian curvatures were calculated across the entire brain of each subject. Mean curvature is equal to half of the sum of the principal curvatures, $(k1 + k2)/2$, and is an extrinsic measure of curvature, which means that it depends on the embedding. Gaussian curvature is equal to the product of the principal curvatures, $(k1*k2)$, and is an intrinsic property of the surface, which means that it does not depend on the particular embedding of the surface. Gaussian and mean curvatures are the most important types of curvatures in surface theory (Abbena et al., 2017).

2.5. Classification using artificial neural networks

Artificial neural networks are widely used to perform classification tasks. In the proposed CAD system, a feedforward neural network with two hidden layers was used to classify the MRA data into two classes based on the extracted features in Section 2.4. One class was for the normotensive subjects and the second was for the hypertensive subjects. We have used the built-in MATLAB R2017a neural network training tool in our experiments. We have used different classifiers with different parameters in our experiment including support vector machine (SVM) with polynomial (cubic) kernel, ensemble bagged trees, linear discriminant, and a 2-hidden layers artificial neural network. In addition, we have tried all possible k-fold cross validation scenarios. The scenario that achieved the best performance and accuracy was the one that employed a 2-hidden layer ANN with hidden layers of sizes 10 and 5, respectively. Data were randomly divided between training, validation, and testing such that 70% of data were used for training, 15% were used for validation (10-fold), and the remaining 15% were used for testing. The network was trained using a scaled conjugate gradient backpropagation. The default values of other parameters of the neural network training built-in tool were used. The inputs for the neural network were the feature vectors produced by the feature extraction step. Each feature vector consisted of 15 values to represent vascular diameter and tortuosity changes. The first eleven values in each feature vector were the PDF bins corresponding to each blood vessel diameter value (represented by blood vessel radius). The remaining four values

were the averages and medians of both mean curvature and Gaussian curvature (representing vascular tortuosity). The motivation behind this stage was to validate the efficacy of the proposed cerebral features (vessel diameters and tortuosity) in representing a discriminatory factor for hypertension detection. This kind of validation could potentially help clinicians to evaluate changes or alterations in these cerebral features as a signal for the development of severe diseases such as hypertension. This would potentially help clinicians in diagnosing prehypertension and treating potential patients with appropriate medical plans.

3. Results

3.1. Segmentation results

To test the accuracy of the 3-D CNN segmentation, the dataset was divided into 49 subjects which were used for training, and the remaining 17 subjects were used for testing. Common segmentation evaluation metrics (Dice similarity coefficient (DSC), sensitivity, and specificity) were used to evaluate the segmentation accuracy. The segmentation approach was successful in delineating cerebral vasculature with $83.2 \pm 2.3\%$ DSC, $83.4 \pm 5.9\%$ sensitivity, and $99 \pm 0.03\%$ specificity compared to experts manually segmented ground truth. We had a hypothesis that partitioning each MRA volume into two compartments to perform the segmentation task locally, (above CoW, at and below CoW) instead of globally (over the entire brain) would potentially address the blood flow signals variability challenge and enhance the segmentation results. To validate the correctness of this hypothesis, two separate experiments were conducted (global, and local) and the results were compared as shown in Fig. 3. The results proved the correctness of our hypothesis as the local segmentation results outperformed the global segmentation results in terms of more detected anatomical details of blood vessels' seeds and fewer gaps between segments of blood vessels. The local experiment achieved $84.4 \pm 3.3\%$ DSC, $86.2 \pm 3.8\%$ sensitivity, and $99 \pm 0.03\%$ specificity compared to ground truth (Table 1). In addition, the 3-D CNN segmentation approach was compared to the global statistical-based approach (GSB) (El-Baz et al., 2012) and the results, presented in Table 1 and shown in Fig. 4, proved the outperformance of

Table 1
Segmentation results of the 3-D CNN approach (local and global experiments) and the global statistical-based approach (GSB)(El-Baz et al., 2012).

Approach	DSC, %	Sensitivity, %	Specificity, %
3D CNN (local)	84.4 ± 3.3	86.2 ± 3.8	99.0 ± 0.03
3D CNN (global)	83.2 ± 2.3	83.4 ± 5.9	99.0 ± 0.03
GSB El-Baz et al. (2012)	80.1 ± 2.7	85.2 ± 3.1	97.5 ± 0.9

our approach. Moreover, the paired *t*-test is used to measure the statistical significance between the obtained results and the other compared techniques. The differences between the metrics means were found to be statistically significant as the corresponding *p*-values are below 0.0001.

It was essential to have accurate segmentation results because this would have a positive impact on the accuracy and efficiency of the extracted features.

3.2. Classification Results

Many experimental trials have been conducted with different classifiers, parameters, kernels, and validation scenarios. A summary of the classification results that recorded accuracy > 80% are shown in Table 2. The best classification process recorded 95.6%, 90%, and 90% for training, validation, and testing, respectively. The confusion matrix for the classification process is shown in Fig. 5 where the overall accuracy was 90.9%. The ROC curve is shown in Fig. 6 with area under the curve (AUC) = 0.9091. Fig. 7 shows the performance of the classifier which depended on minimizing the cross entropy between the three stages of training, validation, and testing. This high accuracy is evidence that the modeled vascular features used to classify subjects were reliable and efficient to quantify cerebral alterations.

3.3. Comparison to current hypertension prediction risk models

Comparison to existing state-of-the-art hypertension prediction risk models has been conducted. We have selected two common risk models used to predict hypertension namely, the Cox proportional hazard model, and the Framingham risk model. The Cox proportional hazard model was fit to our data, with the outcome variable being hypertension at two years post-baseline. Predictor variables included age and BMI at baseline, as well as gender. In addition, three different sets of MRA-derived predictors were tested. The model using the vessel diameter histogram produced no result, the fitting procedure having failed to converge due to small sample size. The model including averaged Gaussian and mean curvatures was not significant (likelihood ratio $\chi^2 = 5.56$ with 5 d.f.; p = 0.351). Likewise, the model including median Gaussian and mean curvatures was not statistically significant (likelihood ratio $\chi^2 = 6.45$ with 5 d.f.; p = 0.265).

Table 2
Classification accuracy of different classifiers(SVM, Ensemble Bagged Trees (ensemble method: Bag), Linear Discriminant, 2-hidden Layer ANN).

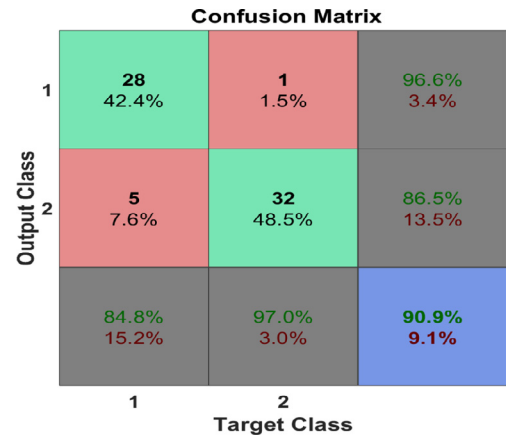| Classifier	Accuracy	Kernel/metric	validation
SVM	80.3%	Polynomial (cubic)	33 − Fold
Ensemble	83.3%	Bagged trees	6 − Fold
Linear Discriminant	84.8%	Linear	33 − Fold
SVM	87.5%	Polynomial (cubic)	10 − Fold
2-hidden Layer ANN	**90.9%**	**FeedForward**	**10 − Fold**

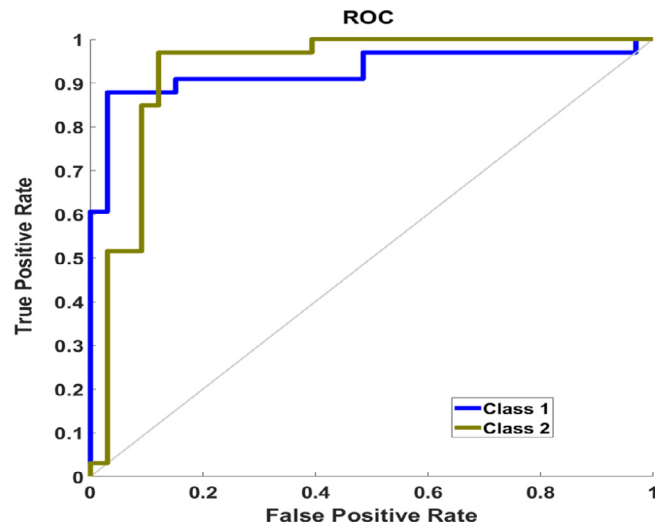**Fig. 5.** The confusion matrix of the classification process.

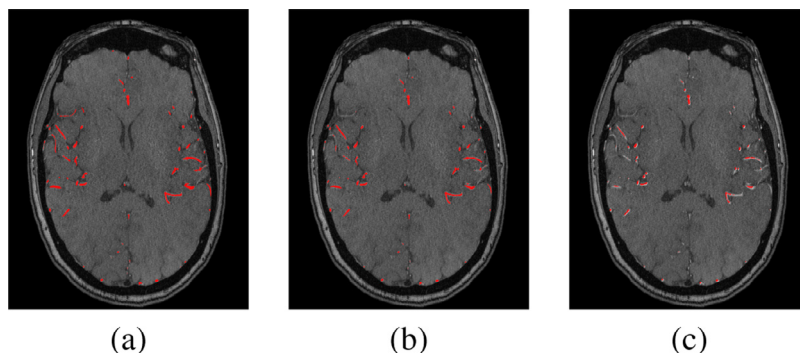**Fig. 6.** The ROC curve of the classifier (AUC = 0.9091).

Fig. 4. A comparison sample of the segmentation approaches. (a) Ground truth, (b) Output of the 3-D CNN approach, (c) Output of the GSB approach (El-Baz et al., 2012).
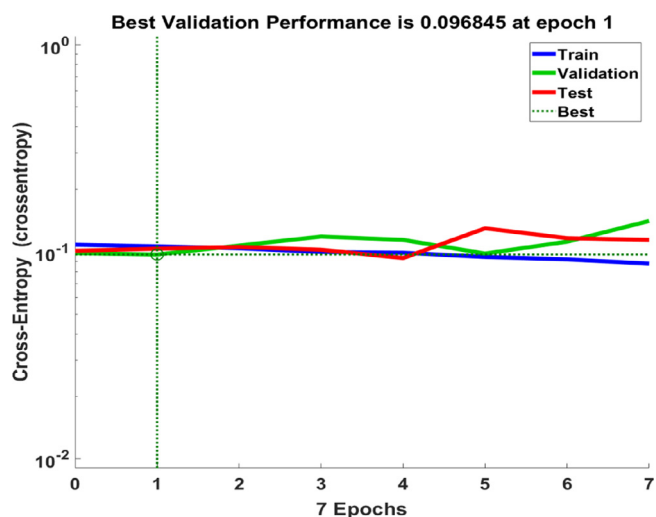
Fig. 7. A plot of the training, validation, and testing performance of the classifier.

Table 3
The confusion matrix of the Framingham prediction model.

		Predicted	
		Normal	Hypertensive
Observed	**Normal**	29	3
	Hypertensive	8	10

For comparison with our predictive model, the Framingham raw scores were calculated for our sample (Parikh et al., 2008). Raw point totals were used rather than the two-year risk score, since the latter was calibrated for a general population while our dataset was selected to have equal numbers of hypertensive and normotensive patients. Instead, two-year hypertension was predicted using logistic regression on the raw point total, and a leave-one-out procedure. The resulting confusion matrix is given in Table 3 (compare Fig. 5).

This comparison indicates the efficacy of our ANN-based classifier to predict hypertension using the proposed MRA features (vascular diameter and tortuosity).

4. Discussion

Common symptoms of hypertension are nose bleeds, headaches, shortness of breath, and vomiting. However, hypertension is called the silent killer because it is common that patients may not experience any apparent symptoms even in advanced stages. Tracking cerebral vasculature would help clinicians in predicting the potentiality of developing hypertension before its onset. Accordingly, clinicians would manage proactive and preventive procedures to avoid the progression of the disease. In this manuscript, a CAD system is presented to help clinicians in the prediction process. The system is capable of distinguishing between normal and hypertensive cases with accuracy of more than 90%, by analyzing the alterations that affect cerebral vascular structures over time efficiently. This demonstrates the efficacy of using the proposed features to represent cerebrovascular changes that precede the onset of hypertension. The high accuracy of the system is evidence that the proposed cerebral features are reliable enough to be used as a diagnostic parameter for predicting the potentiality of developing hypertension. The automatic segmentation algorithm could successfully detect and segment large and small blood vessels and is applicable to either healthy or unhealthy vessels. Previous segmentation algorithm presented in literature were suitable for healthy vessels with assumptions of linearity and circular cross-section (Moccia et al., 2018). Importantly, the proposed segmentation algorithm is fully automatic

which will eliminate possible human errors resulting from intra- and inter-observer variability.

We have carefully selected two features to represent the cerebrovascular alterations based on various studies in literature that support the correlations between the change of vascular diameter and tortuosity, and developing hypertension (Abdalla et al., 2015; Annunziata et al., 2016; Han, 2012; Hayashi et al., 2018; Hiroki et al., 2002; Jakob et al., 1996; Lange et al., 2013; Trucco et al., 2010; Ussavarungsi et al., 2014).

We have exploited the strength of artificial neural networks classifiers to classify the extracted features and decide whether a person is normal or hypertensive. Comparison to common risk models for hypertension prediction has been conducted and the results were evidence to the efficacy of our proposed system to exploit the cerebrovascular features to predict hypertension before its onset. One limitation of this system is that MRA screening is expensive, so we suggest that this system should be used for patients with high potential to develop hypertension due to strong family history of hypertension for example. However, we must refer to the high cost of hypertension medication which is about $ 2000/year. Also, the hospitalization of some common consequent side effects of hypertension such as hemorrhagic stroke is over $32, 000/year (Kirkland et al., 2018; Wang et al., 2014) which makes MRA screening cost effective on the long-term.

5. Data availability

The data that support the findings of this study are available from the corresponding author upon reasonable request.

Author contributions

- H. Kandil, A. Soliman, and A. El-Baz participated in the problem analysis and methodology design.
- F. Taher, M. Ghazal, and R. Keynton provided advising and financial support to conduct the experiments.
- G. Giridharan provided advising and manuscript revision.
- J. Jennings provided advising, data collection and manuscript revision.
- A. El-Baz provided mentorship and advising

Declaration of Competing Interest

The authors declare no competing interests.

References

Abbena, E., Salamon, S., Gray, A., 2017. Modern Differential Geometry of Curves and Surfaces with Mathematica. CRC press.

Abdalla, M., Hunter, A., Al-Diri, B., 2015. Quantifying retinal blood vessels' tortuosity. Science and Information Conference (SAI), 2015. IEEE, pp. 687–693.

Annunziata, R., Kheirkhah, A., Aggarwal, S., Hamrah, P., Trucco, E., 2016. A fully automated tortuosity quantification system with application to corneal nerve fibres in confocal microscopy images. Med. Image Anal. 32, 216–232.

Arimura, H., Li, Q., Korogi, Y., Hirai, T., Abe, H., Yamashita, Y., Katsuragawa, S., Ikeda, R., Doi, K., 2004. Automated Computerized Scheme for Detection of Unruptured Intracranial Aneurysms in Three-dimensional Magnetic Resonance Angiography. Acad. Radiol. 11 (10), 1093–1104.

Arimura, H., Li, Q., Korogi, Y., Hirai, T., Katsuragawa, S., Yamashita, Y., Tsuchiya, K., et al., 2006. Computerized detection of intracranial aneurysms for three-dimensional mr angiography: feature extraction of small protrusions based on a shape-based difference image technique. Med. Phys. 33 (2), 394–401.

Barnes, J.N., Harvey, R.E., Zuk, S.M., Lundt, E.S., Lesnick, T.G., Gunter, J.L., Senjem, M.L., Shuster, L.T., Miller, V.M., Jack, C.R., et al., 2017. Aortic hemodynamics and white matter hyperintensities in normotensive postmenopausal women. J. Neurol. 264 (5), 938–945.

Bouman, C., Sauer, K., 1993. A generalized gaussian image model for edge-preserving map estimation. IEEE Trans. Image Process. 2 (3), 296–310.

Cates, M.J., Dickinson, C.J., Hart, E.C., Paton, J.F., 2012. Neurogenic hypertension and elevated vertebrobasilar arterial resistance: is there a causative link? Curr. Hypertension Reports 14 (3), 261–269.

Chobanian, A.V., Bakris, G.L., Black, H.R., Cushman, W.C., Green, L.A., Izzo Jr, J.L.,

Jones, D.W., Materson, B.J., Oparil, S., Wright Jr, J.T., et al., 2003. The seventh report of the joint national committee on prevention, detection, evaluation, and treatment of high blood pressure: the jnc 7 report. Jama 289 (19), 2560–2571.

Doi, K., 2007. Computer-aided diagnosis in medical imaging: historical review, current status and future potential. Comput. Med. Imag. Graphics 31 (4), 198–211.

El-Baz, A., Elnakib, A., Khalifa, F., El-Ghar, M.A., McClure, P., Soliman, A., Gimelrfarb, G., 2012. Precise segmentation of 3-d magnetic resonance angiography. IEEE Trans. Biomed. Eng. 59 (7), 2019–2029.

Fujita, H., Uchiyama, Y., Nakagawa, T., Fukuoka, D., Hatanaka, Y., Hara, T., Lee, G.N., Hayashi, Y., Ikedo, Y., Gao, X., Zhou, X., 2008. Computer-aided diagnosis: The emerging of three cad systems induced by japanese health care needs. Computer Methodsand Programs in Biomedicine 92 (3), 238–248. https://doi.org/10.1016/j.cmpb.2008.04.003. Medical Imaging and Medical Informatics (MIMI)

Han, H.-C., 2012. Twisted blood vessels: symptoms, etiology and biomechanical mechanisms. J. Vasc. Res. 49 (3), 185–197.

Hayashi, K., Makino, A., Kakoi, D., 2018. Remodeling of arterial wall: response to changes in both blood flow and blood pressure. J. Mech. Behav. Biomed.Mater. 77, 475–484.

Hiroki, M., Miyashita, K., Oda, M., 2002. Tortuosity of the white matter medullary arterioles is related to the severity of hypertension. Cerebrovasc. Diseas. 13 (4), 242–250.

Iadecola, C., Davisson, R.L., 2008. Hypertension and cerebrovascular dysfunction. Cell metabolism 7 (6), 476–484.

Ioffe, S., Szegedy, C., 2015. Batch normalization: accelerating deep network training by reducing internal covariate shift. arXiv preprint arXiv:1502.03167.

Jakob, M., Spasojevic, D., Krogmann, O.N., Wiher, H., Hug, R., Hess, O.M., 1996. Tortuosity of coronary arteries in chronic pressure and volume overload. Catheteriz. Cardiovasc. Interven. 38 (1), 25–31.

Jennings, J.R., Muldoon, M.F., Ryan, C., Gach, H.M., Heim, A., Sheu, L.K., Gianaros, P.J., 2017. Prehypertensive blood pressures and regional cerebral blood flow independently relate to cognitive performance in midlife. J. Am. Heart Assoc. 6 (3), e004856.

Kamnitsas, K., Ledig, C., Newcombe, V.F., Simpson, J.P., Kane, A.D., Menon, D.K., Rueckert, D., Glocker, B., 2017. Efficient multi-scale 3d cnn with fully connected crf for accurate brain lesion segmentation. Med. Image Anal. 36, 61–78.

Kirkland, E.B., Heincelman, M., Bishu, K.G., Schumann, S.O., Schreiner, A., Axon, R.N., Mauldin, P.D., Moran, W.P., 2018. Trends in healthcare expenditures among us adults with hypertension: national estimates, 2003–2014. J. Am. Heart Assoc. 7 (11), e008731.

Kobashi, S., Kondo, K., Hata, Y., 2006. Computer-aided diagnosis of intracranial aneurysms in mra images with case-based reasoning. IEICE Trans. Inf. Syst. 89 (1), 340–350.

Krähenbühl, P., Koltun, V., 2011. Efficient inference in fully connected crfs with gaussian edge potentials. Advances in neural information processing systems. pp. 109–117.

Lange, T.J., Bornia, C., Stiefel, J., Stroszczynski, C., Arzt, M., Pfeifer, M., Hamer, O.W., 2013. Increased pulmonary artery diameter on chest computed tomography can predict borderline pulmonary hypertension. Pulmonary Circul. 3 (2), 363–368.

Launer, L.J., Lewis, C.E., Schreiner, P.J., Sidney, S., Battapady, H., Jacobs, D.R., Lim, K.O., D'Esposito, M., Zhang, Q., Reis, J., et al., 2015. Vascular factors and multiple measures of early brain health: cardia brain mri study. PloS one 10 (3), e0122138.

Miki, S., Hayashi, N., Masutani, Y., Nomura, Y., Yoshikawa, T., Hanaoka, S., Nemoto, M., Ohtomo, K., 2016. Computer-assisted detection of cerebral aneurysms in mr angiography in a routine image-reading environment: effects on diagnosis by radiologists. Am. J. Neuroradiol. 37 (6), 1038–1043. https://doi.org/10.3174/ajnr.A4671.

Moccia, S., De Momi, E., El Hadji, S., Mattos, L.S., 2018. Blood vessel segmentation algorithms-review of methods, datasets and evaluation metrics. Comput. methodsProgr. Biomed. 158, 71–91.

Nakao, T., Hanaoka, S., Nomura, Y., Sato, I., Nemoto, M., Miki, S., Maeda, E., Yoshikawa, T., Hayashi, N., Abe, O., 2018. Deep neural network-based computer-assisted detection of cerebral aneurysms in mr angiography. J. Magn. Reson. Imag. 47 (4), 948–953. https://doi.org/10.1002/jmri.25842.

Parikh, N.I., Pencina, M.J., Wang, T.J., Benjamin, E.J., Lanier, K.J., Levy, D., D'Agostino Sr., R.B., Kannel, W.B., Vasan, R.S., 2008. A risk score for predicting near-term incidence of hypertension: the framingham heart study. Ann. Internal Med. 148 (2), 102–110.

Soler, D., Cox, T., Bullock, P., Calver, D., Robinson, R., 1998. Diagnosis and management of benign intracranial hypertension. Arch. Diseas. childhood 78 (1), 89–94.

Swales, J., 1991. Neurogenic hypertension: a synthesis and review. J. R. Coll. Physic.Lond. 25 (4), 355.

Trucco, E., Azegrouz, H., Dhillon, B., 2010. Modeling the tortuosity of retinal vessels: does caliber play a role? IEEE Trans. Biomed. Eng. 57 (9), 2239–2247.

Tustison, N.J., Avants, B.B., Cook, P.A., Zheng, Y., Egan, A., Yushkevich, P.A., Gee, J.C., 2010. N4itk: Improved n3 bias correction. IEEE Trans. Med. Imag. 29 (6), 1310–1320.

Ussavarungsi, K., Whitlock, J., Lundy, T., Carabenciov, I., Burger, C., Lee, A., 2014. The significance of pulmonary artery size in pulmonary hypertension. Diseases 2 (3), 243–259.

Wang, G., Zhang, Z., Ayala, C., Dunet, D.O., Fang, J., George, M.G., 2014. Costs of hospitalization for stroke patients aged 18–64 years in the united states. J. Stroke Cerebrovasc. Diseas. 23 (5), 861–868.

Warnert, E.A., Rodrigues, J.C., Burchell, A.E., Neumann, S., Ratcliffe, L.E., Manghat, N.E., Harris, A.D., Adams, Z., Nightingale, A.K., Wise, R.G., et al., 2016. Is high blood pressure self-protection for the brain? Circul. Res. 119 (12), e140–e151.

Whelton, P.K., Carey, R.M., Aronow, W.S., Casey, D.E., Collins, K.J., Himmelfarb, C.D., DePalma, S.M., Gidding, S., Jamerson, K.A., Jones, D.W., et al., 2018. 2017 Acc/aha/aapa/abc/acpm/ags/apha/ash/aspc/nma/pcna guideline for the prevention, detection, evaluation, and management of high blood pressure in adults: a report of the american college of cardiology/american heart association task force on clinical practice guidelines. J. Am. Coll. Cardiol. 71 (19), e127–e248.